Assessing spatial heterogeneity of active layer thickness over Arctic-foothills tundra, North Slope Alaska

Jinyang Du[1], K. Arthur Endsley[1], Kazem Bakian Dogaheh[2, 3], John S. Kimball[1], Mahta Moghaddam[3], Thomas A. Douglas[4], Asem Melebari[3], Sepehr Eskandari[3], Jinhyuk Elisha Kim[5], Jane Whitcomb[3], Yuhuan Zhao[3], Sophia Henze[3]

[1]Numerical Terradynamic Simulation Group, W.A. Franke College of Forestry & Conservation, University of Montana, Missoula, MT, 59812, USA
[2]Department of Earth and Environmental Sciences, University of Michigan, Ann Arbor, MI 481019, USA
[3]Ming Hsieh Department of Electrical Engineering, University of Southern California, Los Angeles, CA 90089, USA
[4]U.S. Army Cold Regions Research and Engineering Laboratory, Fort Wainwright, AK, 99703, USA
[5]Department of Earth System Science, University of California, Irvine, California, 92697, USA

Correspondence to: Jinyang Du (jinyang.du@ntsg.umt.edu)

Abstract. Changes in active layer thickness (ALT) are used as an indicator of permafrost degradation. Increases in ALT can lead to increased greenhouse gas emissions, altered hydrology and ecology, ground instability, and a positive climate feedback. Quantifying ALT spatial heterogeneity remains challenging due to the influence of localized variations in terrain, microclimate, snow/soil properties, vegetation cover, and surface disturbances. It is also unclear how local ALT patterns (e.g., sub-meter to 10 m) and mechanisms scale up to broader landscape footprints (e.g., 10 -1000 m) represented from global satellite observations and Earth system models. We assessed ALT spatial heterogeneity in the Arctic-foothills tundra within the North Slope of Alaska through intensive field sampling over four 90 m x 90 m plots, combined with multi-source remote sensing and machine learning (ML). Analysis using field observations and ML revealed that vegetation, surface wetness, subsurface rocks, and micro-topography exert strong influence on 5-m ALT variations, whereas terrain controls dominate (~65% contribution) at coarser 10-m spatial resolution. By leveraging cm-level optical-infrared drone imagery, we further generated 0.1-m ALT maps over a larger 5 km x 5 km region and examined ALT scaling effects. Our analysis showed a quadratic relationship in resolution-dependent uncertainties, characterized by a rapid increase in uncertainties at the sub-meter level (e.g., RMSE normalized by the standard deviation of 0.1m ALT climbed by ~10%), followed by another 10% increase from 1 m to 30 m resolution, and more conservative error increase (~5%) from 30 m to 1,000 m resolution. Our study allows for improved interpretation of remote sensing and process-based ALT simulations for the changing Arctic by clarifying resolution-dependent uncertainties and underlying mechanisms.

1 Introduction

Permafrost in the northern high latitudes is undergoing rapid changes driven by enhanced atmospheric warming at roughly four times the mean global rate (Rantanen et al., 2022). Complex environmental changes that accompany degrading permafrost include widespread earlier spring thawing and lengthening of the thaw season, shifts in seasonal snow cover properties, contrasting wetting and drying patterns, vegetation greening and browning, and increasing disturbances (Heijmans et al., 2022; Foster et al., 2022). Permafrost degradation, which involves active layer (layer on top of permafrost that undergoes seasonal freeze/thaw) thickening, may lead to ground surface deformation (Du et al., 2019). In addition, thawing permafrost could potentially mobilize a vast reservoir of soil organic carbon previously stabilized in perennially frozen ground, resulting in accelerated soil decomposition and greenhouse gas emissions that may further amplify global warming (Turetsky et al., 2020; Schuur et al., 2022; Miner et al., 2022).

Active layer thickness (ALT), defined as "the thickness of the layer of the ground that is subject to annual thawing and freeing in areas underlain by permafrost" (Van Everdingen et al. 1998), is an essential climate variable for monitoring permafrost degradation (Smith and Brown 2009). Accurate mapping of ALT spatial and temporal variability is critical for understanding impacts of climate change and disturbance on the permafrost energy balance, terrestrial water budget, organic matter decomposition, and land-atmosphere carbon exchange (Zhang et al., 2005; Schaefer et al., 2015; Liu et al., 2024). ALT spatial patterns are closely linked to ambient air temperature at regional scales while demonstrating large spatial heterogeneity at local scales due to complex interactions with precipitation, vegetation, slope, aspect, soil and snow properties, topography, and disturbance (Leibman et al., 2012; Widhalm et al., 2017; Loranty et al., 2018; Chen et al., 2019).

Despite the importance of permafrost landscapes in monitoring and projecting Arctic-boreal system changes, there is only limited understanding of high-resolution (e.g., sub-meter to 10 m) ALT patterns and underlying driving factors over the highly heterogeneous permafrost regions due to a paucity of high-resolution ALT measurements. It is also unclear how local ALT patterns and its associated governing mechanisms scale up to the broader landscape when quantified at coarser spatial resolutions (e.g., 10 m-1000 m) using global satellite observations and regional process models (Yi et al., 2020). However, better understanding of the high-resolution patterns, mechanisms, and their scaling effects are needed to clarify permafrost vulnerability and associated feedbacks to climate change, and to improve representation of the hydrological, ecological, and biogeochemical processes of Arctic ecosystems in global Earth system models as well as remote sensing inversion algorithms (Koven et al., 2013; Chen et al., 2019; Hantson et al 2025).

Remote sensing of ALT at high resolutions ranges from relatively direct electromagnetic retrievals from low frequency ground penetrating radar (GPR) to more indirect measures of surface topographic features from Light Detection and Ranging (LiDAR) (Gangodagamage et al., 2014) and soil freeze-thaw (FT) driven land surface deformations from Interferometric synthetic aperture radar (InSAR) measures (Schaefer et al., 2015). The distribution of ALT over ice-wedge polygon landscapes was empirically inferred using relevant topographic features quantified from LiDAR surface elevation measurements and data fusion approaches (Gangodagamage et al., 2014). In addition, the active layer heaves when frozen and subsides when thawed due to denser liquid water than ice. The seasonal vertical ground movement measured using InSAR is thus related to the ALT and ice/water content (Schaefer et al., 2015). Low-frequency (e.g., L- and P-band) microwave measurements are capable of penetrating through vegetation and soil layers and show strong potential for mapping active layer properties, including soil moisture and FT dynamics, organic matter content, and ALT (Tabatabaeenejad et al., 2014; Bakian-Dogaheh et al., 2025). This is due to the strong microwave sensitivity to the changes of soil dielectric properties, which are affected by soil moisture, texture, and freeze/thaw state (Kneisel et al., 2008; Du et al., 2019). In particular, the contrast in dielectric permittivity at the interface between thawed and frozen soil layers may lead to measurable microwave backscattering or reflection signals for estimating ALT (Kneisel et al., 2008). For example, retrieval algorithms were developed by exploiting airborne P-band radar data for ALT mapping in Alaska (Chen et al 2019), which showed favorable retrieval accuracy for ALT up to ~60 cm. Another study on post-fire recovery in tundra regions further confirmed the unique sensitivity of low-frequency airborne radar in detecting the relatively fine-resolution heterogeneity in active layer conditions and post fire recovery that may be missing from coarser-resolution and higher-frequency satellite observations and model simulations (Yi et al., 2021). More recently advanced physics-based computational radar retrieval algorithms have been developed to map the active layer soil organic matter and soil moisture profile of the Arctic-foothills tundra using P-band radar data (Bakian-Dogaheh et al., 2022). In sum, the remote sensing techniques provide information necessary to infer or model ALT.

Considering its dependence on surface conditions (Kelley et al., 2004), ALT can also be indirectly inferred from optical vegetation observations and relatively high-frequency radar backscatter signals considering the ALT dependence on surface conditions using regression analysis (Kelley et al., 2004; Gangodagamage et al., 2014; Widhalm et al., 2017). Recent machine-learning based studies using airborne hyperspectral imaging data achieved meter-level ALT predictions over Interior Alaska with favorable accuracy (Zhang et al., 2021). Thus, complementary information available from multi-sensor and multi-resolution remote sensing provides the basis for developing more effective models and ALT retrievals capable of resolving local patterns and environmental linkages spanning Arctic-boreal permafrost landscapes (Brodylo et al., 2024; Hantson et al 2025).

The objectives of this study were to: 1) assess ALT spatial heterogeneity and scaling properties from 0.1-m to 1000-m resolution within the tundra foothills region of the North Slope of Alaska; and to 2) assess the underlying environmental controls on ALT patterns manifesting at different resolutions and the potential influence of spatial resolution on regional permafrost remote sensing and modeling uncertainty.

2 Study Region

Our study focused on the Imnavait Creek (68.6167° N, 149.3167° W) area within the Alaskan North Slope tundra foothills region (Fig. 1). The study region experiences a cold climate with a mean annual temperature of -7.4°C, ranging from an average of -17°C in January to 9.4°C in July (Schramm et al., 2007). Annual precipitation averages 340 mm, two-thirds of which falls as light rainfall during the summer (Schramm et al., 2007). The dominant vegetation consists of water-tolerant plants like tussock sedges and mosses, grasses and low shrubs (Schramm et al., 2007). Vegetation and soil patterns vary with slope, aspect, and drainage conditions, exhibiting a patchy distribution across the study domain (Hinkel and Nelson, 2003). The region is also characterized by diverse glacial landforms, including deposits, stream networks, and bedrock outcrops (Hinkel and Nelson, 2003). The region has gently rolling terrain, with elevations ranging from ~750 m to 980 m. Vegetation and soil patterns vary with slope, aspect, and drainage conditions, exhibiting a patchy distribution across the study domain (Hinkel and Nelson, 2003). The region is also characterized by diverse glacial landforms, including deposits, stream networks, and bedrock outcrops (Hinkel and Nelson, 2003). Increasing ALT was observed from both in-situ measurements at the Circumpolar Active Layer Monitoring (CALM) sites (https://www2.gwu.edu/∼calm/data/north.htm) and regional ALT records at 1-km resolution, which were generated using machine learning by combining in situ ALT observations with a suite of observational biophysical variables (Liu et al., 2024).

The local study area consisted of four intensively sampled field plots (Plot 3, Plot 4, Plot 5, and Plot 6 in Fig. 1; 90m ×90m each) distributed across an elevation gradient along west facing hill slopes, and surrounded by a larger (5 km by 5 km) landscape domain used for analyzing ALT across different resolutions (Fig.1; Table 1). The field plots are dominated by tussock-forming sedges and moss-lichen mats, along with scattered dwarf birch shrubs, and riparian grasses (Fig. 1-2). The common species identified near the ALT sampling points include dwarf birch (*Betula nana*), alpine blueberry (*Vaccinium uliginosum*), black bearberry (*Arctous* spp.), crowberry (*Empetrum nigrum*), and *Arctostaphylos uva-ursi*, among other less-recognizable species. Our soil coring samples indicated high organic matter content of the topsoil (0-10 cm depth) for Plots 3, 4 and 5, with the respective values of 77.3%, 75.1%, and 71.8%, contrasting with a relatively low value of 45.5% for Plot 6.

Plot 3 and Plot 4 are located on west-facing downhill slopes characterized by gradual elevation changes (10-15 m across the plot), small water tracks, and scattered glacial erratics. Plot 3 is crossed by multiple drainage features that are transverse to the Kuparuk River (Fig. 1). These features are evident in the topography as well as the vegetation, with alternating bands of dwarf willow, grasses, and tussocks. Standing water is present in many places, as are glacial erratics, particularly along the drainage channels. Plot 4 is more homogeneous in vegetation character and height, consisting mostly of grass tussocks and moss, with some larger glacial erratics present.

Plots 5 and 6 are on the east side of the access road and are more level than Plots 3 and 4. Plot 5 is located at a valley bottom and is partitioned by Imnavait Creek, which winds directly through the middle of the plot. Shallow drainage channels transverse to Imnavait Creek are found on the west side of the plot, while the east side is upland and drier. Vegetation cover in Plot 5 follows the typical mix of grasses, mosses, and sedges, with some moss forming humps about 20 cm tall, while shrub density and height increase close to the creek. Along Imnavait Creek there are taller (0.5-1.0 m) birch shrubs and more grasses. Plot 6 is characterized by widespread subsurface rocks (Fig. 1) and overall short-statured grass-sedge tussocks and mosses, lichens, small bunchgrasses, *Arctous spp.*, and alpine blueberry, interrupted by areas of bare rock and gravel. Bare areas are common in the center of the plot.

As part of the NASA Arctic Boreal Vulnerability (ABoVE) field campaign, our study used ABoVE standard projection, which is Canada Albers Equal Area projection, for data visualization and analysis (https://above.nasa.gov/implementation_plan/standard_projection.html).

Table 1. Summary of surface and soil conditions for the sampling plots

Name	Plot 3	Plot 4	Plot 5	Plot 6
Elevation	810 m	846 m	855 m	875 m
vegetation	dwarf willow, grasses, and tussocks	grass tussocks and moss	mix of grasses, mosses, and sedges	grass tussocks and mosses
Organic matter content	77.3%	75.1%	71.8%	45.5%
Unique characteristics	ephemeral, drainage features	homogeneous in vegetation character and height	located in a valley bottom and partitioned by Imnavait Creek	widespread subsurface rocks
ALT	49 cm	39 cm	44 cm	58 cm

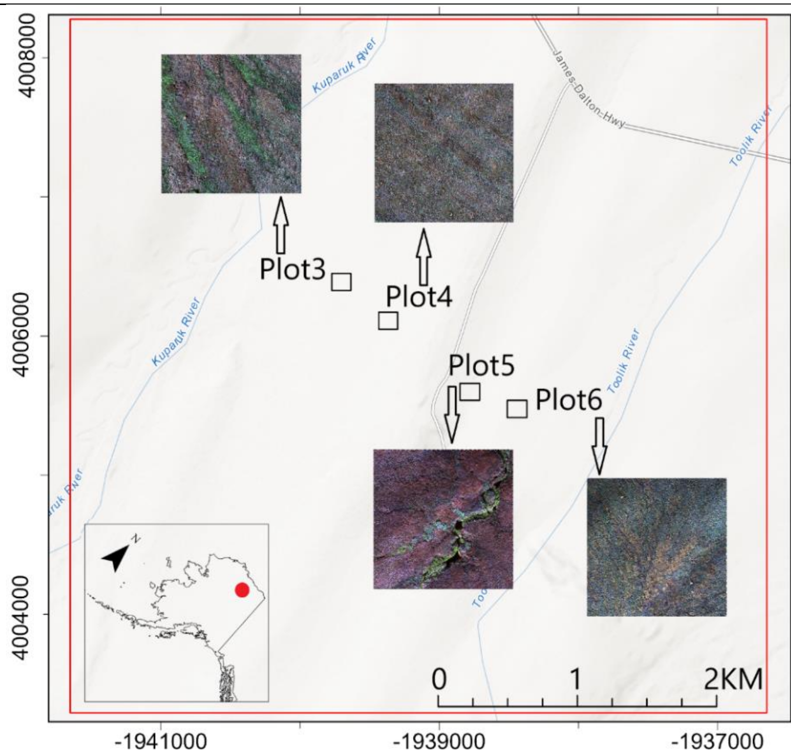

Figure 1: The study region encompasses an Arctic tundra area (68.6167°, -149.3167°; red dot in the inset) in the northern foothills of the Brooks Range, Alaska. The region consists of four intensively sampled plots (Plot 3, Plot 4, Plot 5, and Plot 6; 90 m x 90 m each) with their corresponding true-color RGB (red-green-blue) drone images displayed alongside alongside for visual inspection only, and surrounded by a larger 5km by 5km study region (red rectangle) used for analyzing ALT scaling effects. The map was plotted using Canada Albers Equal Area Conic projection.

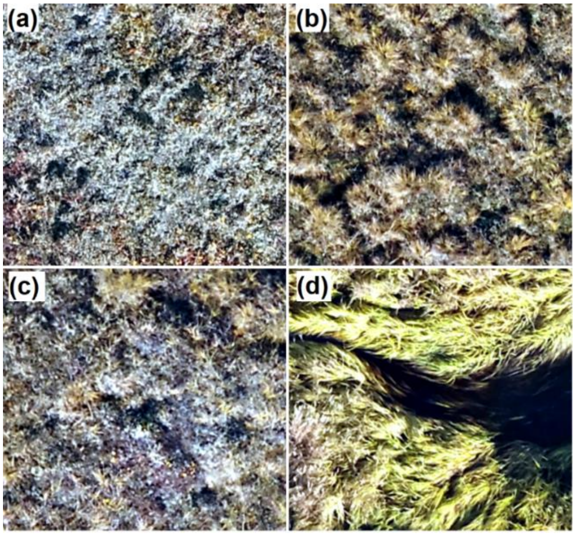

Figure 2: The study region contains characteristic tundra vegetation types, including dwarf shrubs (a), tussock-forming sedges (b), moss-lichen mats (c), and riparian grasses along watercourses (d). The images (0.7cm resolution) were acquired from a drone-based RGB camera.

3 Data and Methods

3.1 Data Sets

Multi-resolution ALT mapping was performed using probe-based field measurements, high-resolution (centimeter level) drone-based optical-Infrared (IR) acquisitions, concurrent airborne L-band radar observations, Sentinel-2 satellite images, and ancillary digital elevation model (DEM) data.

3.1.1 Field Sampling

Ground sampling activities were conducted within the field plots from August 16-23, 2024, which included probe-based ALT measurements, soil coring, and surface roughness measurements. Each plot (Fig. 1) contains 289 grid cells (containing 17 x 17 subpixels with 5 m x 5 m each) excluding a 2.5 m buffer zone along the plot edges. Probe-based ALT sampling was performed over every (or every other) grid cell. Three measurements (by inserting the probe in the active layer vertically until refusal) were taken randomly within each grid cell, unless the initial two measurements were less than 1.27 cm apart. The mechanical probing to the depth of refusal was used to determine the depth of the frost table. For Plot 5, samples were collected for every grid cell not covered by open water, whereas for Plot 6, sampling only covered about half of the area due to widespread shallow rocks. The readings were averaged to represent the ALT conditions for a given 5-m grid cell. Overall, approximately 1700 measurements were made representing ca. 600 grid cells across the plots. Additional observations were made including vegetation types, occurrence of standing and running water, and appearance of subsurface rocks. Soil organic layer properties were also estimated from soil cores taken within the sampling plots (section 2). Field measurement protocols followed previously established methods within the NASA ABoVE field campaign (Schaefer et al., 2021; Bakian-Dogaheh et al., 2022).

3.1.2 Remote Sensing Data Sets

For understanding ALT spatial heterogeneity, multi-resolution remote sensing measurements were collected from drone, piloted aircraft, and satellite platforms. Aerial surveys included drone-based optical-IR observations, and airborne L-band radar observations from the NASA Uninhabited Aerial Vehicle Synthetic Aperture Radar (UAVSAR). The field and airborne data were collected under the ABoVE campaign, an intensive decadal field campaign focused on improving our understanding of climate-related impacts on Arctic and boreal systems in western North America (Miller et al., 2019).

For this study, high-resolution ALT mapping relied on drone-based optical-IR observations from a RGB (red, green, blue) camera (0.7 cm resolution), a Micasense multispectral (blue, green, red, red-edge, near IR bands) camera (2.7 cm resolution), and a DEM (1.2 cm resolution) derived from the RGB imagery. These images were captured over each plot on September 4th, 2024 by the ToolikGIS team from the Toolik Field Station of the University of Alaska Fairbanks. For capturing vegetation conditions and surface water signals, the Normalized Difference Vegetation Index (NDVI; Tucker, 1979) and the Normalized Difference Water Index (NDWI; McFeeters 1996) were calculated respectively from the drone multispectral imagery. In addition, aspect and slope were calculated from the DEM. The drone-based optical images and products were aggregated to both 0.1 m and 5 m resolutions through pixel averaging for supporting the machine learning (ML) and scaling analysis.

For ALT mapping over the surrounding region at coarser spatial resolution, ESA Sentinel-2 satellite optical-NIR observations under clear-sky (cloud cover < 20%) conditions were composited over the summer months (June 15 – August 15, 2024) in Google Earth Engine (GEE). The NDVI and NDWI were derived using the Sentinel-2 observations at 10-m resolution. For understanding terrain controls on the regional ALT distribution, elevation, slope, and aspect data were derived from the ArcticDEM (Porter et al 2018) and aggregated to 10 m resolution.

To examine the possible contributions of airborne radar observations to ALT retrievals, the ML model for 5-m ALT mapping was augmented with additional UAVSAR L-band VV, HV and HH backscatter observations in a separate test. The UAVSAR data were acquired over the Imnavait study region on August 21, 2024 concurrent with the field measurements (Miller et al., 2024). However, the airborne radar data were not used in the scaling analysis, which primarily relied on drone optical imagery for providing cm-level details and Sentinel-2 observations for enabling large-area analysis.

3.2 Constructing Multi-resolution ALT Maps

A multi-resolution approach was used for characterizing ALT spatial heterogeneity, understanding environmental driving factors, and quantifying resolution-dependent uncertainties in remote sensing retrievals. A data-driven Random Forest (RF) model was first trained to reconstruct ALT patterns at a 5-m resolution over the intensively sampled plots. This model was also used with 0.1-m predictors to generate the ALT maps at 0.1 m resolution. The 5-m ALT results were subsequently aggregated to 10-m resolution to train a second RF model, which was used to produce the 10-m ALT map over the surrounding region (Figure 3).

The RF method has been widely used with parameters determined through remote sensing to estimate land parameters such as soil moisture, vegetation optical depth, and ALT (Zhang et al., 2021; Du et al., 2024). The RF tree ensemble yields final regression results by combining individual predictions, resulting in improved accuracy and stability compared to a single tree (Breiman, 2001). Compared with alternative ML methods, the RF demonstrates resilience to data noise and overfitting (Breiman, 2001).

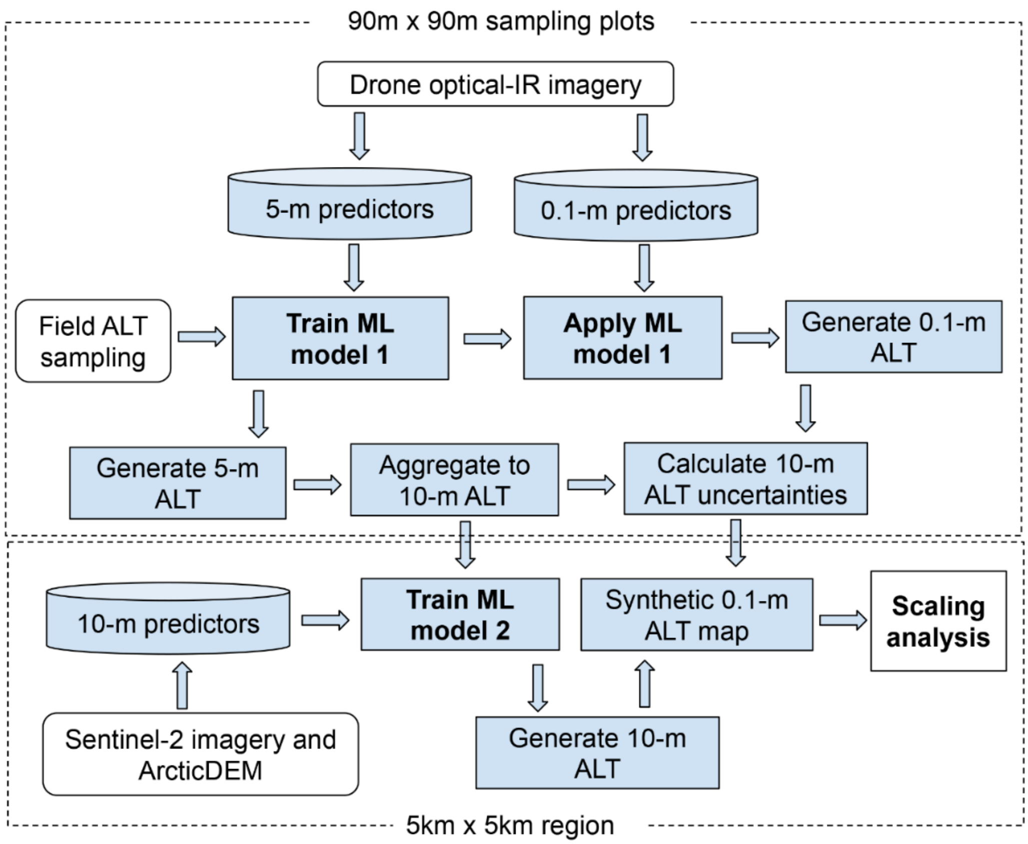

Figure 3: An overall flowchart of the machine learning (ML) based active layer thickness (ALT) mapping and analysis.

For generating the baseline 5-m ALT maps over the sampling plots, the first RF model was trained using the local high-resolution drone optical-NIR imagery, which was aggregated to a coarser (5 m) resolution consistent with the spatial representativeness of the field sampling. The RF target variable is ground-sampled ALT, and the model predictors (Table 2) were selected from different combinations of observations and indices. The model was trained using 80% of the data and validated using 20% of the data. Different sets of hyper-parameters (number of trees 10, 25, 50, 100 and minimum leaf population 1, 3, 5) were employed for tuning and evaluating the regression trees using GEE. The root mean square error (RMSE) and correlation coefficient (R) were calculated for performance evaluation. To reduce overfitting risks, the smaller (larger) value of tree number (minimum leaf population) was selected for prioritizing a relatively simple tree/forest structure if two hyper-parameter values led to similar performance (e.g., R difference less than 0.005). The optimized RF hyper-parameters are 25 trees and a minimum leaf population of 3. The 5-m ALT outputs for the sampling plots from the first RF model were aggregated to 10-m resolution and used to train the second RF model. The second model was developed for regional ALT mapping by leveraging operational satellite data as model predictors. The predictors (Table 2) were selected from terrain features and Sentinel-2 observations. Following a similar dataset splitting and hyper-parameter tuning process, the best performing model was built with a relatively simple structure (10 trees, 1 minimum leaf population).

Table 2. Machine learning predictors for 0.1-m, 5-m, and 10-m ALT mapping and scaling analysis.

Predictors for 5-m and 0.1-m ALT mapping over sampling plots			**Predictors for 10-m ALT mapping over 5 x 5km region**		
Name	Spatial resolution	Drone sensor	Name	Spatial resolution	Data source
R	0.7 cm	RGB Camera	Elevation	2 m	ArcticDEM
G	0.7 cm	RGB Camera	Slope	2 m	ArcticDEM
B	0.7 cm	RGB Camera	Aspect	2 m	ArcticDEM
Red edge	2.7 cm	Multispectral Camera	NDVI	10 m	Sentinel-2
Near infrared	2.7 cm	Multispectral Camera	NDWI	10 m	Sentinel-2
NDVI	2.7 cm	Multispectral Camera			
NDWI	2.7 cm	Multispectral Camera			
Aspect	1.2 cm	RGB Camera			
Slope	1.2 cm	RGB Camera			
Note: Drone images were acquired on 09/04/2024, and the predictors were processed to 0.1-m and 5-m resolutions for the respective ALT mapping.			Note: Terrain data were averaged to 10-m resolution; Satellite images were aggregated over the 2024 summer period from 06/15 to 08/15.		

3.3 Assessing ALT Spatial Heterogeneity

For studying the ALT spatial heterogeneity observed at different resolutions, the first RF model was applied to the drone-based optical-NIR observations aggregated to 0.1m resolution. The 0.1-m ALT maps were generated as a fine-resolution benchmark for evaluating uncertainties in the coarser spatial resolution ALT maps. The 0.1-m ALT maps for the sampling plots were aggregated to 10-m resolution. By comparing the differences between the two maps for each 0.1-m pixel, the estimated RMSE of the 10-m product (referred hereafter as $RMSE_{10m}$) was obtained.

For understanding the ALT variations over larger regions beyond the limited sampling plots, the second RF model was applied using Sentinel-2 and DEM data over the surrounding 5km by 5km area for generating the 10-m ALT regional map. A synthetic 0.1-m ALT map over the surrounding area was then generated using the 10-m ALT map derived from the second RF model and perturbed with noise with a normal distribution and $RMSE_{10m}$ standard deviation.

Multiple ALT regional maps with spatial resolutions ranging from 0.2 to 1000 m were generated by aggregating the 0.1-m pixels of the synthetic map. The aggregation intervals were set as 0.1 m, 1 m, 10 m, and 100 m for deriving the respective maps at sub-meter, meter, decameter, and hectometer resolutions. The uncertainties of a given coarser-resolution map relative to the 0.1-m benchmark were then obtained by calculating their differences over each 0.1-m pixel and measured using two metrics, namely, the relative RMSE normalized by the ALT standard deviation of the 0.1-m data (RMSE/Stdev) and the relative RMSE normalized by the mean ALT (RMSE/mean).

4 Results

4.1 Plot and Regional ALT Mapping

4.1.1 Field Sampling and Multi-source ALT Mapping for the Sampling Plots

The ALT values sampled across all plots have a mean of 45.9 cm and a standard deviation of 11.9 cm. Relatively low ALT (39.3 cm) was typically found in areas dominated by non-riparian shrubs, while larger ALT occurred in soils near standing water (61.0 cm), along creeks (78.2 cm) (e.g., Fig. 4g), and around rocks (70.0 cm) (e.g., Fig. 4j).

The resulting 5-m and 0.1-m ALT maps were compared with the field measurements (Fig. 4). The 5-m ALT maps (Fig.4b, 4e, 4h, 4k) captured the primary ALT patterns observed from the field measurements (Fig. 4a, 4d, 4g, 4j) including elevated ALT along the perimeter of Plot 3, consistently low ALT throughout Plot 4, high ALT values following the water tracks in Plot 5, and generally deep ALT in Plot 6. The 0.1-m results revealed significantly finer variations (Fig. 4c, 4f, 4i, and 4l), resolving ALT patterns associated with small water tracks (e.g., Fig. 4i), discrete vegetation patches (Fig. 4c, 4l), and widespread clusters of underlying rocks (Fig. 4l) that were not discernible at 5-m resolution. Specifically, higher ALT values are visible along

Imnavait Creek within Plot 5, as shown by the red pixels in the field measurements (Fig. 4g), 5-m ML predictions (Fig. 4h), and 0.1-m ML results (Fig. 4i). However, field sampling revealed substantial ALT variation within individual 5-m grid cells, with a standard deviation of up to 32 cm as distance from the watercourse increases. These variations within individual 5-m grid cells are only resolved in the 0.1-m results (Fig. 4i), which distinguish the high ALT values along the creek (red pixels) from the lower values in adjacent areas (blue pixels). Similarly, the stripe patterns of ALT in Plot 4 associated with alternating bands of dwarf willow, grasses, and tussocks (Fig. 1; Section 2) are clearly defined in the 0.1-m predictions (Fig. 4c) but are not discernible in the 5-m results (Fig. 4b). For Plot 6 where overall high ALT is observed (Fig.4 j, 4k, and 4i), heterogeneity is only captured by the 0.1-m results (Fig. 4l). The pattern of interspersed lower-ALT (non-red) pixels within high ALT areas (Fig. 4l) is likely associated with widespread clusters of underlying rocks and complex vegetation cover observed in the field (Fig. 1; Section 2).

Considering the larger ALT variability and more diversified surface conditions at 0.1-m resolution relative to the 5-m resolution, the RF model trained using limited 5-m data set may not be able to fully capture the 0.1-m ALT variations, leading to inconsistency of the overall ALT patterns between the 5-m and 0.1-m results (e.g., Plot 4; Fig. 4d, 4e, 4f) and additional uncertainties in the multi-resolution analysis. In addition, the RF predictions tended to be centralized, which may underestimate larger ALT values (e.g., fewer dark red pixels with ALT higher than 65 cm in Fig. 4h and 4i than the measurements in Fig. 4g) and overestimate smaller ones relative to the measurements (e.g., dark blue pixels with measured ALT smaller than 35 cm in Fig. 4g but not in the ML predictions in Fig. 4h and 4i).

Overall, the first RF model was able to reproduce the sampled ALT at 5-m resolution with a RMSE of 6.53 cm and strong correlation (0.78). Among all the predictors, slope (17.40%), red-edge reflectance (14.05%), aspect (13.44%), and NIR reflectance (12.64%) were the most important features contributing to ALT predictions. The contributions from other predictors including green band (9.91%), blue band (9.43%), NDWI (8.48%), red band (7.41%), and NDVI (7.24%) were also important. The RF model applied to the 0.1-m predictor features was able to capture the high-resolution ALT variability and details missed by coarser-resolution results.

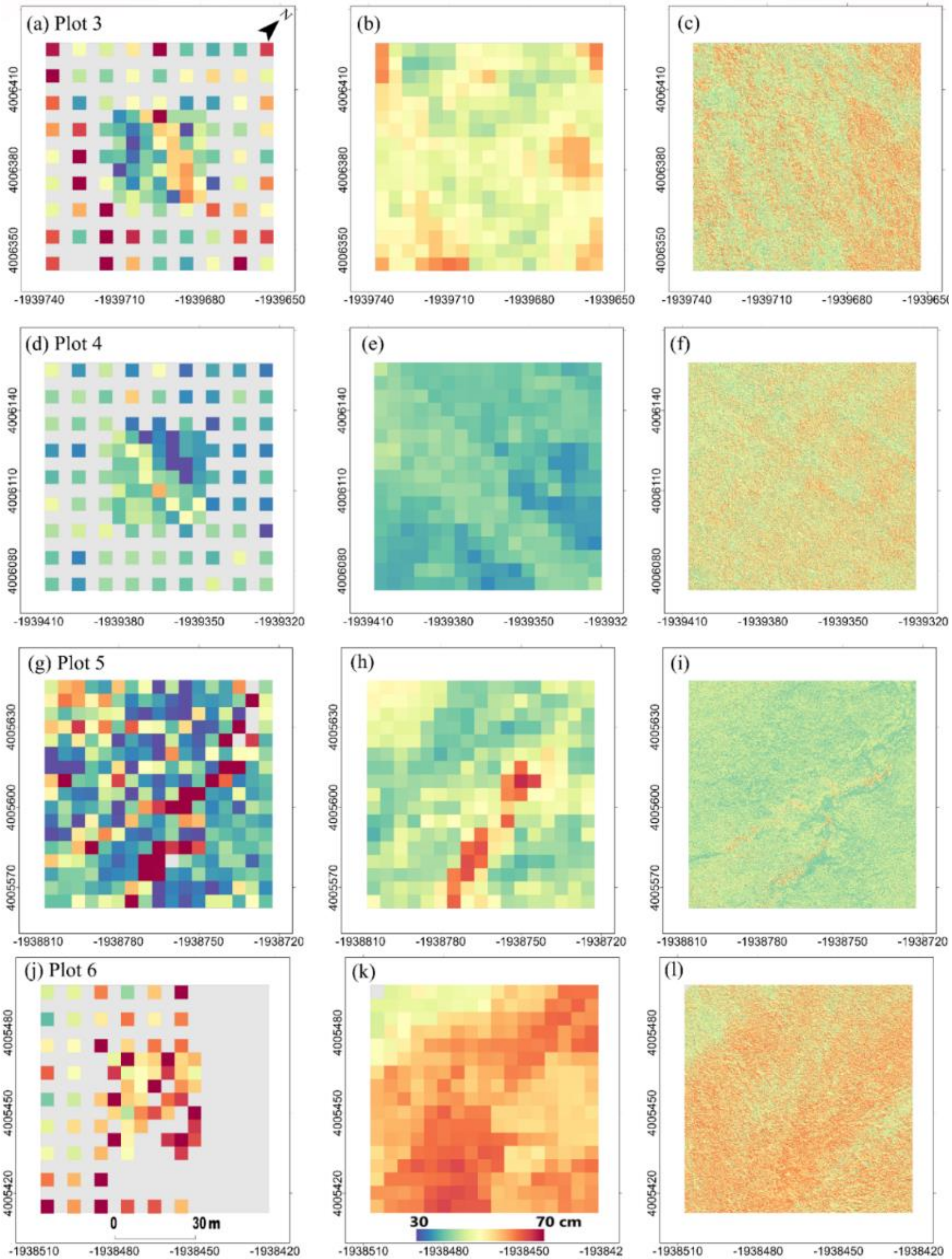

Figure 4: Comparisons of ALT spatial patterns derived from field measurements (a, d, g, j), 5-m machine learning outputs (b, e, h, k), and 0.1-m machine learning estimates (c, f, i, l) for the intensively sampled plots (grey shading indicates areas without sampling). The map was plotted using Canada Albers Equal Area Conic projection.

4.1.2 Satellite-based ALT Mapping over the Surrounding Region

For the second RF model, high accuracy (RMSE 1.63 cm, R 0.97) was achieved for the 10-m ALT predictions over the sampling plots. Terrain factors collectively form the most important control on the ALT distributions at 10-m resolution (elevation 29.88%, aspect 17.85%, slope 17.16%), while vegetation (NDVI 19.85%) and surface wetness (15.26%) conditions are relatively less important.

The model was then applied using Sentinel-2 observations over the larger region surrounding the sampling plots. The resulting regional ALT patterns are strongly influenced by local topography, which is consistent with the RF contribution analysis. The higher-elevation portions of the rolling terrain and gentle hill slopes generally have deeper ALT compared with the steeper slopes (Fig. 5a, 5d) whereas aspect has a secondary role (Fig. 5c).

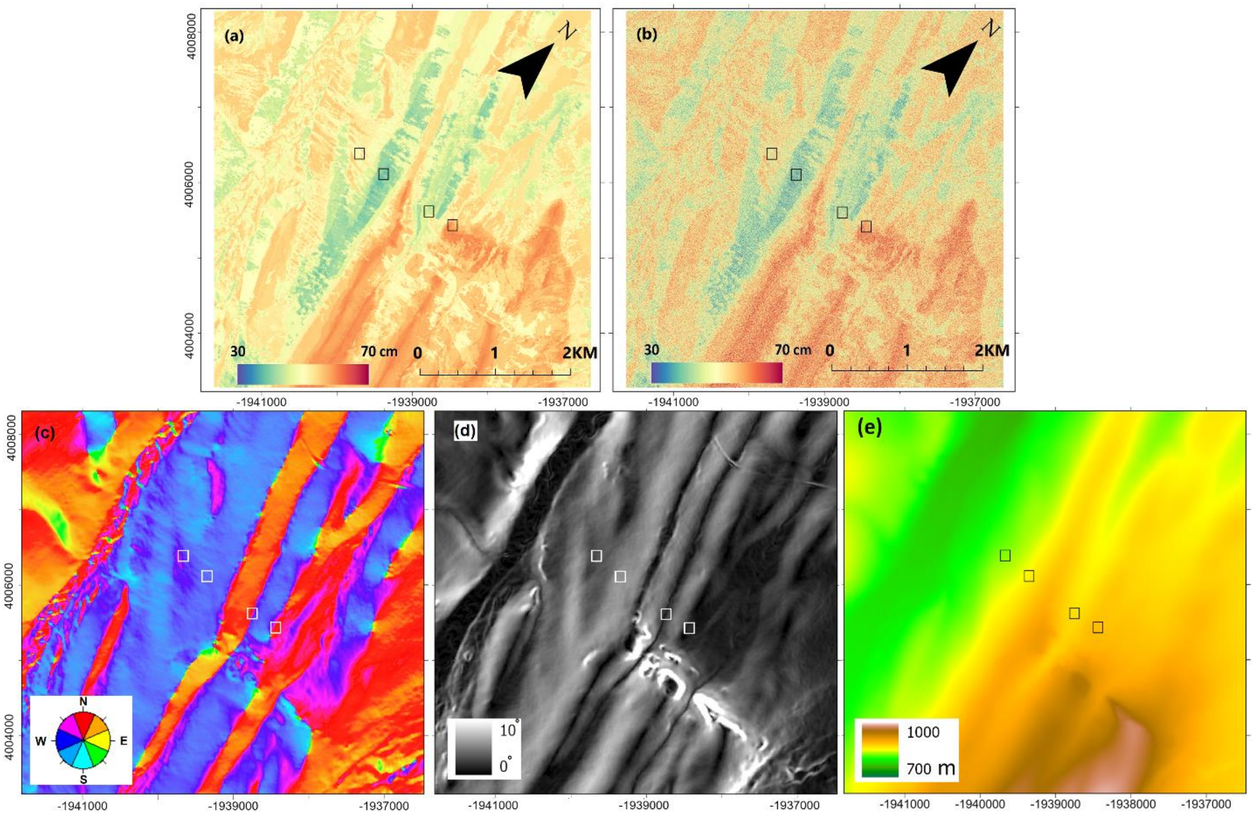

Figure 5: Comparisons between ALT distributions at 10-m resolution derived from machine learning (a), the synthetic ALT map at 0.1-m resolution (b), terrain aspect (c), slope (d), and elevation (e) over a larger 5 km x 5 km area surrounding the sampling plots (black rectangles). The map was plotted using Canada Albers Equal Area Conic projection.

4.2 Resolution-dependent Uncertainties Analysis

The uncertainties associated with coarser-resolution results were calculated by comparing with the synthetic 0.1-m ALT map (Fig. 5b). Uncertainties increase as spatial resolution becomes coarser. However, this increase is most pronounced when moving from high resolutions (e.g., sub-meter to 1 m) and becomes smaller at coarser pixel sizes (e.g., 100 to 1000 m). The increase in ALT uncertainty at coarser spatial resolutions generally follows a quadratic functional form with best fit represented by a second-order polynomial; however, the accelerated error increase at sub-meter resolutions is better characterized by a different second-order polynomial (Fig. 6). The normalized uncertainties (RMSE/Stdev) range from ~68% to 95%, which suggests a majority of the 0.1-m variations are likely smoothed out when observed or modelled at coarser resolutions (e.g., 100-1000 m) (Fig. 6). However, the RMSE magnitudes are relatively small (~9.6% to 13.1%) as compared to the 0.1m ALT mean (Fig. 6).

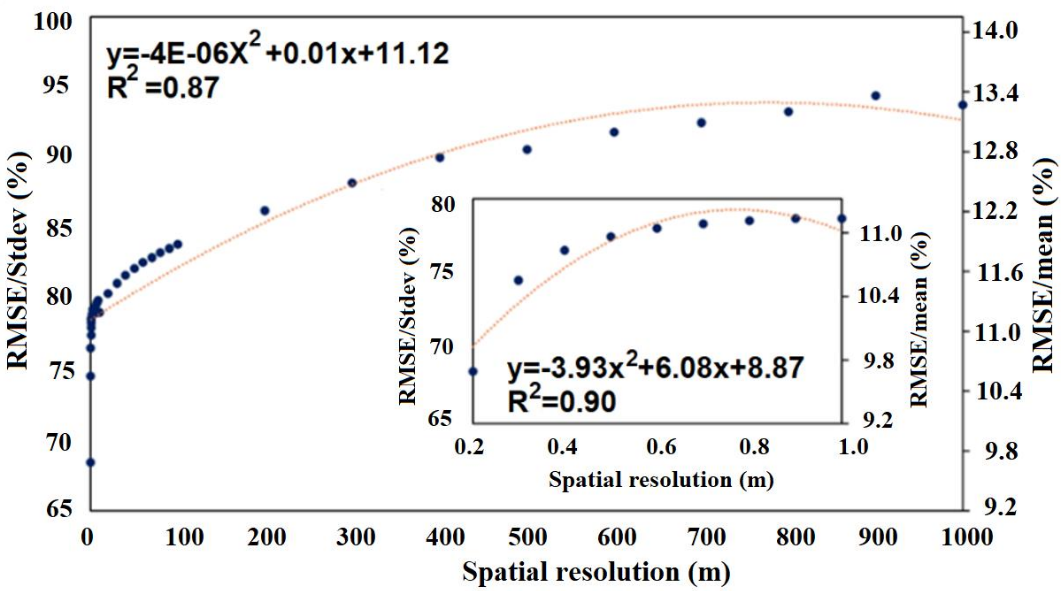

Figure 6: ALT uncertainties change with spatial resolutions from 0.2 to 1000 m with a detailed subset analysis from 0.2 m to 1 m (inset). The uncertainties were determined using the 0.1-m ALT benchmark and normalized by the standard deviation (left vertical axis) and mean (right vertical axis; fitted polynomial function) of the 0.1-m ALT values.

5. Discussion

Recent studies have focused on resolving multi-resolution ALT patterns and their environmental linkages using multi-sensor remote sensing (Brodylo et al., 2024; Hantson et al., 2025). Compared with the existing studies, our study differs in three respects, which include (a) advancing from transect-based (1-dimensional) sampling to intensive 2-dimensional grid-cell sampling, which provided a more comprehensive representation of spatial variability to support multi-resolution analysis; (b) characterizing ALT patterns in the unique Arctic-foothills tundra environment, thereby complementing existing studies for Interior Alaska (Brodylo et al. 2024) and the Seward Peninsula (Hantson et al. 2025); and (c) quantifying resolution-dependent uncertainties in ALT retrievals, offering additional support for improved interpretation of multi-resolution ALT products derived from remote sensing and process-based simulations for the changing Arctic.

5.1 Key Factors Controlling ALT Spatial Variations

Regional ALT dynamics at kilometer or coarser resolutions are primarily governed by air temperature, which affects surface temperature, and further influences soil thermal regimes and therefore active layer conditions (Gangodagamage et al., 2014; Peng et al., 2023). Local ALT variations at finer resolutions (sub-meter to 100 m) are highly complex (Gangodagamage et al., 2014) since soil thermal regimes are further modified by local environmental factors that fine-tune the microclimate. Here, vegetation conditions, snow cover properties, soil texture, soil moisture, surface water bodies, groundwater flow, micro-topography, and disturbances collectively determine the high-resolution ALT pattern (Gangodagamage et al., 2014; Grünberg et al., 2020; Rushlow et al., 2020; Clayton et al., 2021).

Consistent with previous studies, our field observations and RF estimates (section 4.1.1) confirmed that greater ALT is most common in areas with standing water or adjacent to creeks (e.g., Plot 5; Fig. 4g, 4h, 4i), where wet conditions enhance soil thermal conductivity in foothills tundra (Grant et al., 2017; Clayton et al., 2021) despite increased latent heat required for thawing. Relatively larger ALT was also found in the vicinity of subsurface rocks (e.g., within 1-m distance) (e.g., Plot 6; Fig. 5j, 5k, 5l), whose high thermal conductivities facilitate heat propagation and summer thawing (Bonnaventure et al., 2013). Relatively lower ALT was recorded under shrubs, which likely cool the ground in summer through canopy shading (Lawrence and Swenson, 2011) and in winter through the thermal bridging effect (Domine et al., 2022). However, shrubs can also have a counteracting influence on ALT by promoting snow accumulation; whereby, the deeper snow layer insulates the ground, leading to warmer winter soil temperatures (e.g., Palmer et al., 2012; Morse et al., 2012; Kropp et al., 2020) which can result in a deeper active layer when this winter warming effect outweighs the summer shading effect of the shrubs (Way and Lapalme, 2021). A thick moss layer may also slow active layer thaw through its insulating capacity (Schuuring et al., 2024), though no specific descriptions of the moss layer were made in our sampling.

In the Imnavait Creek area, the thickness of the organic layer increases from hill crests to foot slopes. The thicker organic layer provides enhanced thermal insulation, leading to a shallower active layer downhill (Walker and Walker, 1996). Accordingly, Plots 3 and 4 on west-facing downhill slopes and Plot 5 in the valley bottom exhibited overall high soil organic matter content (~75%) and relatively low ALT (~44 cm). In contrast, the higher-elevation Plot 6 had lower organic matter (~46%) and a higher ALT (~58 cm). Besides terrain-controlled organic matter distribution, topography also affects ALT through its impacts on runoff and drainage, soil temperature, snow properties, and vegetation types (Walker and Walker, 1996, Li et al., 2017). Accordingly, topography information including slope (17.40%) and aspect (13.44%) are among the most important factors shaping ALT variations in the ML- and drone-based analysis, while surface features including vegetation, water bodies, and soil properties determined from the multi-spectral reflectance and optical-NIR indices, all showed important contributions to the 5-m ALT predictions over the sampling plots (7.24% to 14.05%; section 4.1.1).

To assess the impact of DEM choice on 5-m ALT predictions, we compared drone-based DEM and ArcticDEM across the four plots. The two DEMs were highly correlated (R = 0.99), though ArcticDEM showed a positive bias of approximately 5.1 m. Nevertheless, ALT predictions derived from ArcticDEM performed nearly as well as the drone-based benchmark, with RMSE increasing slightly from 6.53 cm to 7.24 cm, and correlation decreasing from 0.78 to 0.72.

It is noted that additional radar (L-band 1.26 GHz) observations from UAVSAR helped to enhance the performance of the first RF model (e.g., R increased from 0.78 to 0.81), but were not used in the subsequent scaling analysis (section 3.1.2). For the features selected for radar-based ALT predictions, red-edge reflectance (16.67%), HV-polarized radar backscatter (16.04%), aspect (15.33%), and HH-polarized radar backscatter (15.04%) contributed most to the predictions, while the red band (13.34%), slope (11.99%), and green band (11.57%) observations were relatively less important. The sensitivity of radar backscatter to vegetation biomass, surface water bodies, and soil wetness likely enhanced the ALT estimation.

For the ML- and satellite-based analysis, terrain factors (elevation, slope, and aspect) collectively dominate the ALT predictions (64.89% contribution) at 10-m resolution. The broad ALT patterns over the surrounding region (Fig. 5a) largely align with terrain-driven variability (section 4.1.2), as also observed in a previous study (Hinkel and Nelson, 2003). In general, south-facing slopes in the Northern Hemisphere receive more solar radiation than north-facing slopes, leading to warmer soil and larger ALT. However, the study region is characterized by gentle terrain slopes and west facing aspects (Fig. 5). Besides the terrain-controlled organic matter distribution observed over the Imnavait Creek area, direct solar radiation loading is higher around the hill tops and lower in downslope areas (Hinkel and Nelson, 2003), thus promoting larger ALT conditions in the uplands (Fig. 5). Topography therefore exerts a direct influence on the general thaw pattern as shown in the regional ML analysis.

Based on the Circumpolar Arctic Vegetation Map (CAVM) (Raynolds et al., 2019), plot 3 and 4 belong to vegetation type G3 (Non-tussock sedge, dwarf-shrub, moss tundra) while plot 5 and 6 belong to vegetation type S1 (Erect dwarf-shrub, moss tundra), where G3 and S1 together represent 29.8% area of the Arctic (excluding glacier and water bodies). The Arctic here was defined as the “area of the Earth with tundra vegetation, an arctic climate and arctic flora, with the tree line defining the southern limit” (Raynolds et al., 2019). Accordingly, the model, parameter importance and scaling effects are more suitable for representing the Arctic G3 and S1 areas relative to other regions. However, the study area is also unique in its abundance of glacier deposits and low rolling terrain. For a more rigorous assessment of the applicability or transferability of the data-driven model for other regions, in-situ measurements over a few spatially-distributed regions within the Arctic would be necessary.

In addition, the ALT inter-annual variations are affected by many dynamic factors (e.g., air temperature, snow cover properties, and disturbances), which are not explicitly accounted for by the current model. Multi-season ALT measurements and inclusion of temporally variant predictors in the data-driven model would help extend the current approach and better capture the ALT inter-annual dynamics.

5.2 ALT Resolution-dependent Uncertainties

Quantifying ALT uncertainties associated with varying spatial resolutions of observation and modeling is needed for determining the validity of remote sensing based ALT products, improving permafrost models and simulations, and understanding future climate-ecosystem-hydrology feedbacks (Hantson et al., 2025). Our analysis revealed a greater increase in ALT spatial uncertainty at the sub-meter resolutions (e.g., RMSE/stdev climbed by ~10%), followed by another 10% increase from 1-30 m resolution, and more conservative error growth (~5%) from 30 m to 1000 m resolution. Additional variogram analysis on the 0.1m ALT results further showed the range or correlation length can be as small as 0.86m (e.g., upper-left part of the sampling area of Plot 3; Fig. 4c), suggesting that fine-structure active layer features can be quantified by the methodology. High resolution (e.g., meter or sub-meter level) observations are therefore needed for quantifying the high-resolution ALT heterogeneity, which is consistent with the findings from a discontinuous permafrost region in the Alaskan Seward Peninsula (Hantson et al., 2025).

On the other hand, the scaling effects follow a quadratic form represented by a second-order polynomial function (Fig. 6), which approaches greater error stability at coarser resolutions (e.g., 30-1000 m) and with relatively low RMSE/mean values (e.g., <13.4%). These results indicate that while high-resolution heterogeneities are smoothed out at coarser resolutions, broader ALT patterns remain detectable from relatively coarser satellite observations (e.g., from Sentienl-2, Hantson et al., 2025; MODIS, Liu et al., 2024) and with acceptable error margins to reveal critical active layer dynamics and inform regional process models.

6 Conclusions

This study represents a multi-resolution assessment of ALT spatial heterogeneity within the Arctic foothills of northern Alaska, a region characterized by continuous permafrost cover and complex terrain. We employed a machine learning framework for ALT mapping ranging from local plot (0.1 m) to landscape (10 m) and regional (30-1000 m) levels using multi-resolution observations, including intensive field sampling, and drone, airborne and satellite remote sensing.

Our study showed that vegetation, soil, surface water, and topography are all key drivers of meter-resolution ALT patterns, while terrain topography becomes increasingly dominant in controlling ALT distribution at coarser resolutions. Resolution effect analysis further revealed a quadratic functional relationship describing the growth of resolution-dependent uncertainties in ALT mapping, indicating rapid increase in uncertainty at sub-meter resolutions, moderate error increase at intermediate (1-10 m) resolutions, and more conservative growth at coarser (30-1000 m) resolutions representative of many global satellite and model based assessments. For areas where soil, vegetation, and terrain conditions are markedly different from the Arctic foothills tundra, their ALT scaling effects can be independently quantified through similar approaches from this study.

Code and Data availability. The data that support the findings of this study are in the process of archival and will be openly available through the Oak Ridge National Laboratory Distributed Active Archive Center (ORNL DAAC) (https://doi.org/10.3334/ORNLDAAC/2473). Code used in this study is available upon request.

Author Contributions. JD wrote the manuscript. JD, KAE,KBD,AM,SE,JEK collected field data for analysis. JD, KAE,KBD, JSK, MM, TAD contributed to the design and conceptualization. All coauthors contributed to writing and editing of the manuscript. All coauthors have read and agreed to the published version of this manuscript.

Competing interests. We declare no competing interests are present.

Acknowledgements. This work was conducted at the University of Montana and University of Southern California with funding from the National Aeronautics and Space Administration (80NSSC22K1238). The optical-IR drone images were collected by the Toolik GIS team. The UAVSAR images were provided through the NASA ABoVE airborne campaign.

References

Bakian-Dogaheh, K., Chen, R. H., Yi, Y., Kimball, J. S., Moghaddam, M., and Tabatabaeenejad, A.: A model to characterize soil moisture and organic matter profiles in the permafrost active layer in support of radar remote sensing in Alaskan Arctic tundra, Environ. Res. Lett., 17, 025011, https://doi.org/10.1088/1748-9326/ac4e37, 2022.

Bakian-Dogaheh, K., Zhao, Y., Kimball, J. S., and Moghaddam, M.: Coupled hydrologic-electromagnetic framework to model permafrost active layer organic soil dielectric properties, Remote Sens. Environ., 318, 114560, https://doi.org/10.1016/j.rse.2024.114560, 2025.

Bonnaventure, P. P. and Lamoureux, S. F.: The active layer: A conceptual review of monitoring, modelling techniques and changes in a warming climate, Prog. Phys. Geogr., 37, 352–376, https://doi.org/10.1177/0309133313478314, 2013.

Breiman, L.: Random forests, Mach. Learn., 45, 5–32, https://doi.org/10.1023/A:1010933404324, 2001.

Brodylo, D., Douglas, T. A., and Zhang, C.: Quantification of active layer depth at multiple scales in Interior Alaska permafrost, Environ. Res. Lett., 19, 034013, https://doi.org/10.1088/1748-9326/ad264b, 2024.

Chen, R. H., Tabatabaeenejad, A., and Moghaddam, M.: Retrieval of permafrost active layer properties using time-series P-band radar observations, IEEE Trans. Geosci. Remote Sens., 57, 6037–6054, https://doi.org/10.1109/TGRS.2019.2903935, 2019.

Clayton, L. K., Schaefer, K., Battaglia, M. J., Bourgeau-Chavez, L., Chen, J., Chen, R. H., Chen, A., Bakian-Dogaheh, K., Grelik, S., Jafarov, E., and Liu, L.: Active layer thickness as a function of soil water content, Environ. Res. Lett., 16, 055028, https://doi.org/10.1088/1748-9326/abfa4c, 2021.

Domine, F., Fourteau, K., Picard, G., Lackner, G., Sarrazin, D., and Poirier, M.: Permafrost cooled in winter by thermal bridging through snow-covered shrub branches, Nat. Geosci., 15, 554–560, https://doi.org/10.1038/s41561-022-00979-2, 2022.

Du, J., Watts, J. D., Jiang, L., Lu, H., Cheng, X., Duguay, C., Farina, M., Qiu, Y., Kim, Y., Kimball, J. S., and Tarolli, P.: Remote sensing of environmental changes in cold regions: Methods, achievements and challenges, Remote Sens., 11, 1952, https://doi.org/10.3390/rs11161952, 2019.

Du, J., Kimball, J. S., Guo, J. S., Kannenberg, S. A., Smith, W. K., Feldman, A., and Endsley, A.: Enhanced satellite monitoring of dryland vegetation water potential through multi-source sensor fusion, Geophys. Res. Lett., 51, e2024GL110385, https://doi.org/10.1029/2024GL110385, 2024.

Foster, A. C., Wang, J. A., Frost, G. V., Davidson, S. J., Hoy, E., Turner, K. W., Sonnentag, O., Epstein, H., Berner, L. T., Armstrong, A. H., and Kang, M.: Disturbances in North American boreal forest and Arctic tundra: impacts, interactions, and responses, Environ. Res. Lett., 17, 113001, https://doi.org/10.1088/1748-9326/ac98d7, 2022.

Gangodagamage, C., Rowland, J. C., Hubbard, S. S., Brumby, S. P., Liljedahl, A. K., Wainwright, H., Wilson, C. J., Altmann, G. L., Dafflon, B., Peterson, J., and Ulrich, C.: Extrapolating active layer thickness measurements across Arctic polygonal terrain using LiDAR and NDVI data sets, Water Resour. Res., 50, 6339–6357, https://doi.org/10.1002/2013WR014283, 2014.

Grant, R. F., Mekonnen, Z. A., Riley, W. J., Wainwright, H. M., Graham, D., and Torn, M. S.: Mathematical modelling of arctic polygonal tundra with ecosys: 1. Microtopography determines how active layer depths respond to changes in temperature and precipitation, J. Geophys. Res. Biogeosci., 122, 3161–3173, https://doi.org/10.1002/2017JG004037, 2017.

Grünberg, I., Wilcox, E. J., Zwieback, S., Marsh, P., and Boike, J.: Linking tundra vegetation, snow, soil temperature, and permafrost, Biogeosciences, 17, 4261–4279, https://doi.org/10.5194/bg-17-4261-2020, 2020.

Hantson, W., Yang, D., Serbin, S. P., Fisher, J. B., and Hayes, D. J.: Scaling Arctic landscape and permafrost features improves active layer depth modeling, Environ. Res. Ecol., 4, 015001, https://doi.org/10.1088/2752-664X/ad9f6c, 2025.

Heijmans, M. M., Magnússon, R. Í., Lara, M. J., Frost, G. V., Myers-Smith, I. H., van Huissteden, J., Jorgenson, M. T., Fedorov, A. N., Epstein, H. E., Lawrence, D. M., and Limpens, J.: Tundra vegetation change and impacts on permafrost, Nat. Rev. Earth Environ., 3, 68–84, https://doi.org/10.1038/s43017-021-00233-0, 2022.

Hinkel, K. M. and Nelson, F. E.: Spatial and temporal patterns of active layer thickness at Circumpolar Active Layer Monitoring (CALM) sites in northern Alaska, 1995–2000, J. Geophys. Res. Atmos., 108, 8168, https://doi.org/10.1029/2001JD000927, 2003.

Kelley, A. M., Epstein, H. E., and Walker, D. A.: Role of vegetation and climate in permafrost active layer depth in arctic tundra of northern Alaska and Canada, J. Glaciol. Geocryol., 26, 269–274, 2004.

Kneisel, C., Hauck, C., Fortier, R., and Moorman, B.: Advances in geophysical methods for permafrost investigations, Permafr. Periglac. Process., 19, 157–178, https://doi.org/10.1002/ppp.616, 2008.

Koven, C. D., Riley, W. J., and Stern, A.: Analysis of permafrost thermal dynamics and response to climate change in the CMIP5 Earth System Models, J. Clim., 26, 1877–1900, https://doi.org/10.1175/JCLI-D-12-00228.1, 2013.

Kropp, H., Loranty, M. M., Natali, S. M., Kholodov, A. L., Rocha, A. V., Myers-Smith, I., Abbot, B. W., Abermann, J., Blanc-Betes, E., Blok, D. and Blume-Werry, G.: Shallow soils are warmer under trees and tall shrubs across Arctic and Boreal ecosystems, Environmental research letters, 16(1), p.015001, https://doi.org/10.1088/1748-9326/abc994, 2020.

Lawrence, D. M. and Swenson, S. C.: Permafrost response to increasing Arctic shrub abundance depends on the relative influence of shrubs on local soil cooling versus large-scale climate warming, Environ. Res. Lett., 6, 045504, https://doi.org/10.1088/1748-9326/6/4/045504, 2011.

Leibman, M. O., Khomutov, A. V., Orekhov, P. T., Khitun, O. V., Epstein, H., Frost, G., and Walker, D. A.: Gradient of seasonal thaw depth along the Yamal transect, Proc. Tenth Int. Conf. Permafr., 25, 237–242, 2012.

Li, A., Tan, X., Wu, W., Liu, H. and Zhu, J.: Predicting active-layer soil thickness using topographic variables at a small watershed scale, Plos one, 12(9), p.e0183742, 2017, https://doi.org/10.1371/journal.pone.0183742.

Liu, Z., Kimball, J. S., Ballantyne, A., Watts, J. D., Natali, S. M., Rogers, B. M., Yi, Y., Klene, A. E., Moghaddam, M., Du, J., and Zona, D.: Widespread deepening of the active layer in northern permafrost regions from 2003 to 2020, Environ. Res. Lett., 19, 014020, https://doi.org/10.1088/1748-9326/ad0f73, 2024.

Loranty, M. M., Abbott, B. W., Blok, D., Douglas, T. A., Epstein, H. E., Forbes, B. C., Jones, B. M., Kholodov, A. L., Kropp, H., Malhotra, A., and Mamet, S. D.: Reviews and syntheses: Changing ecosystem influences on soil thermal regimes in northern high-latitude permafrost regions, Biogeosciences, 15, 5287–5313, https://doi.org/10.5194/bg-15-5287-2018, 2018.

McFeeters, S. K.: The use of the Normalized Difference Water Index (NDWI) in the delineation of open water features, Int. J. Remote Sens., 17, 1425–1432, https://doi.org/10.1080/01431169608948714, 1996.

Miller, C. E., Griffith, P. C., Goetz, S. J., Hoy, E. E., Pinto, N., McCubbin, I. B., Thorpe, A. K., Hofton, M., Hodkinson, D., Hansen, C., Woods, J., and co-authors: An overview of ABoVE airborne campaign data acquisitions and science opportunities, Environ. Res. Lett., 14, 080201, https://doi.org/10.1088/1748-9326/ab0d44, 2019.

Miller, C. E., Griffith, P. C., Hoy, E., Pinto, N. S., Lou, Y., Hensley, S., Chapman, B. D., Baltzer, J., Bakian-Dogaheh, K., Bolton, W. R., Bourgeau-Chavez, L., and co-authors: The ABoVE L-band and P-band airborne synthetic aperture radar surveys, Earth Syst. Sci. Data, 16, 2605–2624, https://doi.org/10.5194/essd-16-2605-2024, 2024.

Miner, K. R., Turetsky, M. R., Malina, E., Bartsch, A., Tamminen, J., McGuire, A. D., Fix, A., Sweeney, C., Elder, C. D., and Miller, C. E.: Permafrost carbon emissions in a changing Arctic, Nature Reviews Earth & Environment, 3, 55-67, https://doi.org/10.1038/s43017-021-00230-3, 2022.

Morse, P. D., Burn, C. R., and Kokelj, S. V.: Influence of snow on near-surface ground temperatures in upland and alluvial environments of the outer Mackenzie Delta, Northwest Territories, Canadian Journal Earth Sciences, 49: 895-913. https://doi.org/10.1139/E2012-012, 2012.

Palmer, M. J., Burn, C. R., and Kokelj, S. V.: Factors influencing permafrost temperatures across tree line in the uplands east of the Mackenzie Delta, 2004–2010, Canadian Journal of Earth Sciences, 49: 877-894. https://doi.org/10.1139/E2012-002, 2012.

Peng, X., Zhang, T., Frauenfeld, O. W., Mu, C., Wang, K., Wu, X., Guo, D., Luo, J., Hjort, J., Aalto, J., and Karjalainen, O.: Active layer thickness and permafrost area projections for the 21st century, Earth's Future, 11, e2023EF003573, https://doi.org/10.1029/2023EF003573, 2023.

Porter, C., Morin, P., Howat, I., Noh, M. J., Bates, B., Peterman, K., Keesey, S., Schlenk, M., Gardiner, J., Tomko, K., and Willis, M.: ArcticDEM [Data set], Harvard Dataverse, https://doi.org/10.7910/DVN/OHHUKH, 2018.

Rantanen, M., Karpechko, A. Y., Lipponen, A., Nordling, K., Hyvärinen, O., Ruosteenoja, K., Vihma, T., and Laaksonen, A.: The Arctic has warmed nearly four times faster than the globe since 1979, Commun. Earth Environ., 3, 168, https://doi.org/10.1038/s43247-022-00498-3, 2022.

Raynolds, M. K., Walker, D. A., Balser, A., Bay, C., Campbell, M., Cherosov, M. M., Daniëls, F. J., Eidesen, P. B., Ermokhina, K. A., Frost, G. V. and Jedrzejek, B.: A raster version of the Circumpolar Arctic Vegetation Map (CAVM), Remote Sensing of Environment, 232, p.111297, https://doi.org/10.1016/j.rse.2019.111297, 2019.

Rushlow, C. R., Sawyer, A. H., Voss, C. I., and Godsey, S. E.: The influence of snow cover, air temperature, and groundwater flow on the active-layer thermal regime of Arctic hillslopes drained by water tracks, Hydrogeol. J., 28, 2057–2069, https://doi.org/10.1007/s10040-020-02166-2, 2020.

Schaefer, K., Liu, L., Parsekian, A., Jafarov, E., Chen, A., Zhang, T., Gusmeroli, A., Panda, S., Zebker, H. A., and Schaefer, T.: Remotely sensed active layer thickness (ReSALT) at Barrow, Alaska using interferometric synthetic aperture radar, Remote Sens., 7, 3735–3759, https://doi.org/10.3390/rs70403735, 2015.

Schaefer, K., Clayton, L. K., Battaglia, M. J., Bourgeau-Chavez, L. L., Chen, R. H., Chen, A. C., Chen, J., Bakian-Dogaheh, K., Douglas, T. A., Grelick, S. E., and Iwahana, G.: ABoVE: Soil moisture and active layer thickness in Alaska and NWT, Canada, 2008–2020, ORNL DAAC, Oak Ridge, Tennessee, USA, https://doi.org/10.3334/ORNLDAAC/1903, 2021.

Schramm, I., Boike, J., Bolton, W. R., and Hinzman, L. D.: Application of TopoFlow, a spatially distributed hydrological model, to the Imnavait Creek watershed, Alaska, J. Geophys. Res. Biogeosci., 112, G04S41, https://doi.org/10.1029/2006JG000326, 2007.

Schuuring, S., Halvorsen, R., Bronken Eidesen, P., Niittynen, P., Kemppinen, J., and Lang, S. I.: High Arctic vegetation communities with a thick moss layer slow active layer thaw, J. Geophys. Res. Biogeosci., 129, e2023JG007880, https://doi.org/10.1029/2023JG007880, 2024.

Schuur, E. A., Abbott, B. W., Commane, R., Ernakovich, J., Euskirchen, E., Hugelius, G., Grosse, G., Jones, M., Koven, C., Leshyk, V., and Lawrence, D.: Permafrost and climate change: Carbon cycle feedbacks from the warming Arctic, Annu. Rev. Environ. Resour., 47, 343–371, https://doi.org/10.1146/annurev-environ-012220-011847, 2022.

Smith, S. and Brown, J.: Assessment of the status of the development of the standards for the Terrestrial Essential Climate Variables-T7-Permafrost and seasonally frozen ground, Global Terrestrial Observing System GTOS 62, Food and Agriculture Organization of the United Nations (FAO), Rome, 2009.

Tabatabaeenejad, A., Burgin, M., Duan, X., and Moghaddam, M.: P-band radar retrieval of subsurface soil moisture profile as a second-order polynomial: First AirMOSS results, IEEE Trans. Geosci. Remote Sens., 53, 645–658, https://doi.org/10.1109/TGRS.2014.2326839, 2014.

Tucker, C. J.: Red and photographic infrared linear combinations for monitoring vegetation, Remote Sens. Environ., 8, 127–150, https://doi.org/10.1016/0034-4257(79)90013-0, 1979.

Turetsky, M. R., Abbott, B. W., Jones, M. C., Anthony, K. W., Olefeldt, D., Schuur, E. A., Grosse, G., Kuhry, P., Hugelius, G., Koven, C., and Lawrence, D. M.: Carbon release through abrupt permafrost thaw, Nat. Geosci., 13, 138–143, https://doi.org/10.1038/s41561-019-0526-0, 2020.

Van Everdingen, R.O. ed.: Multi-language glossary of permafrost and related ground-ice terms in Chinese, English, French, German, Icelandic, Italian, Norwegian, polish, Romanian, Russian, Spanish, and Swedish. International Permafrost Association, Terminology Working Group, 1998.

Walker, D. A. and Walker, M. D.: Terrain and vegetation of the Imnavait Creek watershed, Landscape function and disturbance in Arctic Tundra, pp. 73-108, Berlin, Heidelberg: Springer Berlin Heidelberg, 1996.

Way, R. G., and Lapalme, C. M.: Does tall vegetation warm or cool the ground surface? Constraining the ground thermal impacts of upright vegetation in northern environments, Environmental Research Letters, 16: 054077. https://doi.org/10.1088/1748-9326/abef31, 2021

Widhalm, B., Bartsch, A., Leibman, M., and Khomutov, A.: Active-layer thickness estimation from X-band SAR backscatter intensity, Cryosphere, 11, 483–496, https://doi.org/10.5194/tc-11-483-2017, 2017.

Yi, Y., Kimball, J. S., Watts, J. D., Natali, S. M., Zona, D., Liu, J., Ueyama, M., Kobayashi, H., Oechel, W., and Miller, C. E.: Investigating the sensitivity of soil heterotrophic respiration to recent snow cover changes in Alaska using a satellite-based permafrost carbon model, Biogeosciences, 17, 5861–5882, https://doi.org/10.5194/bg-17-5861-2020, 2020.

Yi, Y., Chen, R. H., Moghaddam, M., Kimball, J. S., Jones, B. M., Jandt, R. R., Miller, E. A., and Miller, C. E.: Sensitivity of multifrequency polarimetric SAR data to postfire permafrost changes and recovery processes in Arctic tundra, IEEE Trans. Geosci. Remote Sens., 60, 1–15, https://doi.org/10.1109/TGRS.2021.3125715, 2021.

Zhang, C., Douglas, T. A., and Anderson, J. E.: Modeling and mapping permafrost active layer thickness using field measurements and remote sensing techniques, Int. J. Appl. Earth Obs. Geoinf., 102, 102455, https://doi.org/10.1016/j.jag.2021.102455, 2021.

Zhang, T., Frauenfeld, O. W., Serreze, M. C., Etringer, A., Oelke, C., McCreight, J., Barry, R. G., Gilichinsky, D., Yang, D., Ye, H., and Ling, F.: Spatial and temporal variability in active layer thickness over the Russian Arctic drainage basin, J. Geophys. Res. Atmos., 110, D16102, https://doi.org/10.1029/2004JD005642, 2005.